molecules

MDPI

Article

A Site-Ordered Quadruple Perovskites, $RMn_3Ni_2Mn_2O_{12}$ with R = Bi, Ce, and Ho, with Different Degrees of B Site Ordering

Alexei A. Belik

Research Center for Materials Nanoarchitectonics (MANA), National Institute for Materials Science (NIMS), Namiki 1-1, Tsukuba 305-0044, Ibaraki, Japan; alexei.belik@nims.go.jp

Abstract: A site-ordered quadruple perovskites, $AA'_3B_4O_{12}$, can have 3*d* transition metals at A′ and B sites, and show complex magnetic interactions and behavior. Additional complexity appears when B site-ordered arrangements are realized in $AA'_3B_2B'_2O_{12}$. In this work, A site-ordered quadruple perovskites, $RMn_3Ni_2Mn_2O_{12}$ with R = Bi, Ce, and Ho, were prepared by a high-pressure, high-temperature method at about 6 GPa and about 1500 K. The R = Bi and Ce samples were found to crystallize in space group *Im*-3 with a disordered distribution of Ni^{2+} and Mn^{4+} cations in one B site. On the other hand, the R = Ho sample crystallized in space group *Pn*-3 and showed partial ordering of Ni^{2+} and Mn^{4+} cations between two B sites. The structural data (and bond valence sums) suggest that cerium has the oxidation state +3, which is unusual for such perovskites. Magnetic properties were investigated by magnetic susceptibility and specific heat measurements, which showed the presence of one magnetic transition near 36 K for R = Bi; there was evidence for the presence of two magnetic transitions near 27 K and 33 K for R = Ce, and near 10 K and 36 K for R = Ho. Curie–Weiss parameters were estimated for all samples from high-temperature magnetic measurements up to 750 K. The total effective magnetic moment for R = Ce also suggests the presence of Ce^{3+}. A magnetic field of 90 kOe had the largest effect on the specific heat of the R = Ho sample, and almost no effects on the specific heat of the R = Bi sample.

Keywords: A site-ordered quadruple perovskites; B site double ordering; crystal structures; structural disorder; magnetic properties

Academic Editor: Takashiro Akitsu

Received: 27 March 2025
Revised: 10 April 2025
Accepted: 11 April 2025
Published: 14 April 2025

Citation: Belik, A.A. A Site-Ordered Quadruple Perovskites, $RMn_3Ni_2Mn_2O_{12}$ with R = Bi, Ce, and Ho, with Different Degrees of B Site Ordering. *Molecules* **2025**, *30*, 1749. https://doi.org/10.3390/molecules30081749

1. Introduction

Simple perovskite oxides, ABO_3, usually have non-magnetic A cations (such as, Ca^{2+}, Sr^{2+}, Ba^{2+}, Pb^{2+}, La^{3+}, Y^{3+}, and Bi^{3+}) or magnetic rare-earth cations [1–5]. Therefore, the magnetism of ABO_3 perovskites is primarily driven by B cations (if they are magnetic). Even if both A and B cations are magnetic, they behave separately at higher temperatures, and the interaction between A and B cations is weak. For example, $RFeO_3$ perovskites have Fe^{3+} ordering at about 600–740 K, while R^{3+} ordering takes place below about 10 K [6].

On the other hand, A site-ordered quadruple perovskites, $AA'_3B_4O_{12}$, have a small square-planar A′ site, which usually accommodates 3*d* transition metals [7–11]. Therefore, such perovskites can show complex magnetic interactions and behavior and much stronger interactions between cations in the A′ and B sites. Additional complexity can appear when different cations are located at the B sites. Depending on the size and charge difference [2], B site-ordered arrangements can be realized, leading to the general formula for such perovskites being $AA'_3B_2B'_2O_{12}$ [12–28]. High degrees of B site cation orders are usually realized when the charge difference between B and B′ cations is higher than 3, or when

there is a large difference in the electronic properties between B and B′ cations [2]. When the charge difference between B and B′ cations is equal to 2, synthesis conditions start to play a very important role in the degree of cation order [2].

Special attention has been given in the literature to perovskite-related compounds with B = Ni^{2+} and B′ = Mn^{4+} [29–46], because such a combination is expected to give ferromagnetic (FM) interactions according to the Goodenough–Kanamori rules [47]. The charge difference between Ni^{2+} and Mn^{4+} is 2; therefore, it is often challenging to obtain fully ordered samples.

Simple R_2NiMnO_6 perovskites can be prepared at ambient pressure from R = La to R = Lu. The degree of Ni^{2+} and Mn^{4+} ordering has significant effects on the FM properties of R_2NiMnO_6 [35–38] and on the saturation magnetization values. In nearly ordered samples, T_C (T_C is an FM Curie temperature) decreases almost linearly from 280 K for R = La [30,36] to 40 K for to R = Lu [12,44,45]. Such changes in T_C correlate with changes in the Ni–O–Mn bond angles. Further reduction in the Ni–O–Mn bond angle results in dramatic changes in magnetic interactions and properties. For example, Sc_2NiMnO_6, even with full ordering of Ni^{2+} and Mn^{4+}, shows two antiferromagnetic (AFM) transitions and a complex magnetodielectric response [41]. In_2NiMnO_6, also with full ordering of Ni^{2+} and Mn^{4+}, demonstrates a complex incommensurate AFM structure below T_N = 26 K (T_N is an AFM Néel temperature) and spin-induced ferroelectric polarization at T_N [39,40]. As Lu_2NiMnO_6 appears to be located near a phase boundary between FM and AFM ground states, a moderate pressure can change Ni–O–Mn bond angles enough to induce a transition from an FM ground state to an incommensurate AFM ground state [44]. It should be noted that Sc_2NiMnO_6 and In_2NiMnO_6 can only be prepared using a high-pressure, high-temperature method.

Peculiarities of both the R_2NiMnO_6 and $AA'_3B_2B'_2O_{12}$ perovskite families are combined in the case of $LaMn_3Ni_2Mn_2O_{12}$ [12], which can be prepared only using a high-pressure, high-temperature method. $LaMn_3Ni_2Mn_2O_{12}$ is located in a region of a phase diagram with unusual properties similar to those of Sc_2NiMnO_6 and In_2NiMnO_6. For example, two magnetic transitions were found in $LaMn_3Ni_2Mn_2O_{12}$ at 34 K and 46 K with original magnetic structures [12,13]. Such perovskites were recently extended to $RMn_3Ni_2Mn_2O_{12}$ with R = Nd, Sm, Gd, and Dy [48], which can also be prepared only using a high-pressure, high-temperature method.

In this work, we investigated $RMn_3Ni_2Mn_2O_{12}$ with R = Bi, Ce, and Ho. Bi-containing perovskites are exceptional members of any perovskite family [49–53] in the majority of cases, as a Bi^{3+} cation has the lone electron pair and promotes polar distortions. Ce usually has the oxidation state of +4; therefore, Ce-containing members of any perovskite family may differ from other members of the same series with R^{3+}. Perovskites with different oxidation states of Ce are reported in the literature [54–62]. Ho^{3+} is the smallest cation for which $RMn_3Ni_2Mn_2O_{12}$ perovskites have been prepared so far.

2. Results and Discussion

All prepared $RMn_3Ni_2Mn_2O_{12}$ samples with R = Bi, Ce, and Ho had a cubic crystal structure, as all reflections belonging to $RMn_3Ni_2Mn_2O_{12}$ could be indexed in a cubic system. The samples also contained different impurities depending on R: the R = Bi sample had $Bi_2O_2CO_3$, NiO, $NiMnO_3$, and $GdFeO_3$-type impurities, the R = Ce had CeO_2, NiO, and $NiMnO_3$ impurities, and the R = Ho sample had $HoMn_2O_5$, NiO, and $NiMnO_3$ impurities. All cubic reflections of the R = Bi and Ce samples could be indexed in space group *Im*-3, which is the parent (maximum) symmetry of the $AA'_3B_4O_{12}$-type perovskites [7–11]. On the other hand, a (311) reflection was observed in the synchrotron XRPD data of the R = Ho sample (the inset of Figure 1a). This reflection is forbidden in space group *Im*-3, and

suggests space group *Pn*-3, which is observed in cases of full or partial B site ordering of $AA'_3B_2B'_2O_{12}$-type perovskites [12,14–19].

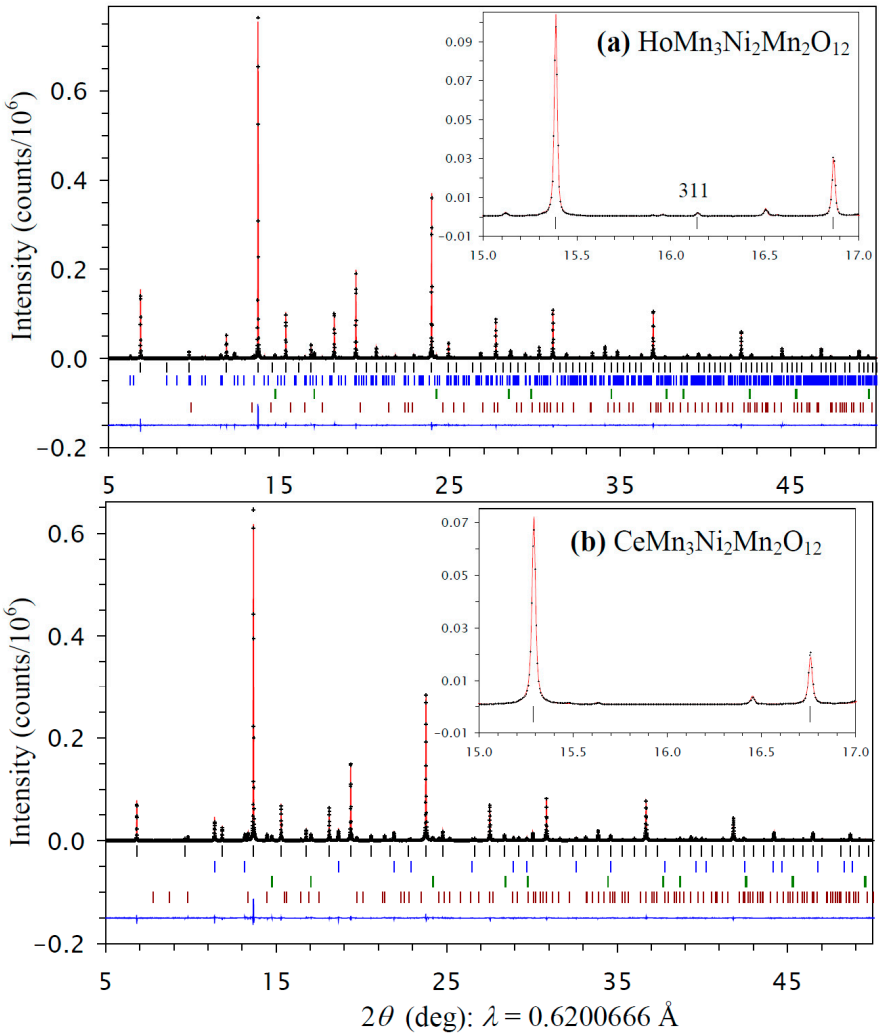

Figure 1. Fragments of experimental (black crosses), calculated (red line), and difference (blue line at the bottom) room-temperature synchrotron X-ray powder diffraction patterns of (**a**) $HoMn_3Ni_2Mn_2O_{12}$ (the *Pn*-3 modification) and (**b**) $CeMn_3Ni_2Mn_2O_{12}$ (the *Im*-3 modification) in a 2θ range of 5° and 50°. The tick marks show possible Bragg reflection positions for the main phase (black) and impurities (from top to bottom for $HoMn_2O_5$ (blue), NiO (green), and $NiMnO_3$ (brown) for R = Ho and for CeO_2 (blue), NiO (green), and $NiMnO_3$ (brown) for R = Ce). Insets show magnified parts in a 2θ range of 15° and 17°, and emphasize the presence of the (311) reflection for R = Ho from the B site ordering and the absence of such a reflection for R = Ce.

The distribution of Ni^{2+} and Mn^{4+} cations between the B and B′ sites in the R = Ho sample was refined with the following constraints: (1) the full site occupation, g(Mn) + g(Ni) = 1, where g is the occupation factor, should be kept, and (2) the total chemical composition should be kept. The obtained distribution of Ni^{2+} and Mn^{4+} cations was close to $0.8Ni^{2+} + 0.2Mn^{4+}$ for the B site and $0.2Ni^{2+} + 0.8Mn^{4+}$ for the B′ site. These values suggest a significant degree of Ni^{2+} and Mn^{4+} ordering. We note that similar distributions of Ni^{2+} and Mn^{4+} cations were found in samples with R = Nd, Sm, Gd, and Dy [48] prepared under the same conditions.

The refinement of the occupation factors of the R sites (together with atomic displacement parameters (ADPs) of the R sites and all other refined parameters) gave the following values: g(Bi) = 1.0001(13), g(Ce) = 0.9710(15), and g(Ho) = 0.9929(14). These values were

close to 1 within the sensitivity of the method, as such deviations could be absorbed by reasonable ADPs. Therefore, we fixed the occupation factor of the R sites at 1 in the final reported models. We emphasize that the ADP for Bi was enhanced. However, all attempts to split (to reduce the ADP of Bi) the Bi site from the ideal (0, 0, 0) position to different positions failed. Enhanced ADPs for Bi are often observed in such perovskites with a cubic structure, even in neutron diffraction data [52]. Enhanced ADPs for Bi are caused by the effect of the lone electron pair of Bi^{3+} cations and random displacements of Bi^{3+} cations.

The refined structural parameters of $HoMn_3Ni_2Mn_2O_{12}$ are summarized in Table 1, and those of $RMn_3Ni_2Mn_2O_{12}$ with R = Bi and Ce in Table 2. Experimental, calculated, and difference synchrotron X-ray powder diffraction patterns are shown in Figure 1 for $HoMn_3Ni_2Mn_2O_{12}$ and $CeMn_3Ni_2Mn_2O_{12}$. Figure S1 gives experimental, calculated, and difference synchrotron X-ray powder diffraction patterns for $BiMn_3Ni_2Mn_2O_{12}$.

Table 1. Structural parameters of $HoMn_3Ni_2Mn_2O_{12}$ (*Pn*-3; prepared at 1500 K) at room temperature from synchrotron powder X-ray diffraction data.

Site	WP	*g*	*x*	*y*	*z*	B_{iso} (Å^2)
Ho	2*a*	1	0.25	0.25	0.25	0.685(6)
Mn_{SQ}	6*d*	1	0.25	0.75	0.75	0.507(9)
Ni_1/Mn_1	4*b*	0.815(12)Ni + 0.185Mn	0	0	0	0.31(3)
Mn_2/Ni_2	4*c*	0.815Mn + 0.185Ni	0.5	0.5	0.5	0.29(3)
O	24*h*	1	0.2578(4)	0.4242(2)	0.5567(2)	0.56(3)

Note. Crystal system: cubic; space group *Pn*-3 (No. 201, setting 2); $Z = 2$. Source: synchrotron powder X-ray diffraction (λ = 0.6200666 Å); *d*-space range used in refinements: 0.4678–7.108 Å. $a = 7.32452(1)$ Å, $V = 392.9504(9)$ Å^3. WP: Wyckoff position. $R_{wp} = 9.24\%$, $R_p = 6.29\%$, $R_I = 2.48\%$, and $R_F = 2.35\%$ after background subtraction. $R_{wp} = 6.34\%$, $R_p = 4.62\%$, $R_I = 3.16\%$, and $R_F = 3.49\%$ without background subtraction. Occupation factors, *g*, of Ho, Mn_{SQ}, and O sites are 1. Constraints on occupation factors: $g(Mn_1) = g(Ni_2) = 1 - g(Ni_1)$ and $g(Mn_2) = g(Ni_1)$. Impurities: NiO—2.5 wt. %, $HoMn_2O_5$—3.2 wt. %, and $NiMnO_3$—0.4 wt. %.

The bond valence sum (BVS) values [63,64] of the Mn_{SQ} site (where SQ stands for square-planar) were close to +3 for all three compounds (+2.94 for R = Bi, +2.97 for R = Ce, and +2.95 for R = Ho) suggesting that this site is occupied by Mn^{3+} cations. The BVS values of the Ni/Mn site (with $R_0 = 1.7035$, which is the average value of $R_0(Ni^{2+})$ and $R_0(Mn^{4+})$ [63]) were +2.90 for R = Bi and +2.89 for R = Ce, again close to the average oxidation state of Ni^{2+} and Mn^{4+} cations. On the other hand, for R = Ho, the BVS value of the Ni_1/Mn_1 site (with the majority of Ni^{2+}) was +2.28, and the BVS value of the Mn_2/Ni_2 site (with the majority of Mn^{4+}) was +3.98, in agreement with the expected values. The BVS value of the Ni_1/Mn_1 site was somewhat higher than +2; however, similar values were observed in all other members of the $RMn_3Ni_2Mn_2O_{12}$ family with R = La [12], Nd, Sm, Gd, and Dy [48].

The BVS values of the R site were +2.71 for R = Bi, +3.04 for R = Ce [64], and +2.63 for R = Ho. Reduced BVS values of Bi^{3+} cations are often observed in Bi-containing A site-ordered quadruple perovskites [49,52], and could be caused by the influence of the lone electron pair of Bi^{3+} cations. The BVS value for Ho^{3+} suggests that Ho^{3+} cations are highly underbonded inside the A site. The severe underbonding could be a reason why $RMn_3Ni_2Mn_2O_{12}$ compounds become unstable with smaller R^{3+} cations [65], such as with R = Er-Lu [48], under the synthesis conditions used. In $RMn_3Ni_2Mn_2O_{12}$, the BVS values of R^{3+} cations changed from +3.40 for R = La [12] to +2.72 for R = Dy [48]. Therefore, the BVS value for R = Ho agrees with the general tendency in such perovskites. These BVS values also suggest that cations at the A site can be highly overbonded or highly underbonded, but the structure can still tolerate such stress. Stabilization of the structure was realized through the high-pressure, high-temperature preparation method. The BVS value for Ce suggests that Ce has an oxidation state of +3. Therefore, the reduction of Ce^{4+} (added as

CeO_2) took place during the synthesis of $CeMn_3Ni_2Mn_2O_{12}$, and $CeMn_3Ni_2Mn_2O_{12}$ is not an exceptional member of the $R^{3+}Mn_3Ni_2Mn_2O_{12}$ series. The reduction of Ce^{4+} occurred through the oxidation of a part of Mn^{3+}, as the high-pressure synthesis was performed in sealed capsules in closed environment.

Table 2. Structural parameters of $RMn_3Ni_2Mn_2O_{12}$ (*Im*-3; prepared at 1500 K) at room temperature from synchrotron powder X-ray diffraction data.

R	Bi	Ce
Wavelength (Å)	0.4137875	0.6200666
Used *d*-space range (Å)	0.3122–11.855	0.4678–7.108
a (Å)	7.37294(1)	7.37071(1)
V (Å^3)	400.7949(11)	400.4314(7)
B_{iso}(R) (Å^2)	2.095(9)	0.565(9)
B_{iso}(Mn_{SQ}) (Å^2)	0.624(12)	0.521(12)
B_{iso}(Ni/Mn) (Å^2)	0.436(8)	0.280(9)
x(O)	0.31118(22)	0.31053(20)
y(O)	0.17728(24)	0.17562(22)
B_{iso}(O) (Å^2)	0.83(4)	0.62(3)
R_{wp} (%)	7.54 (6.22)	8.48 (6.76)
R_p (%)	5.37 (4.56)	5.73 (4.96)
R_I (%)	3.37 (3.49)	2.87 (3.67)
R_F (%)	5.99 (6.03)	1.58 (2.59)
Impurities:		
NiO	1.9 wt. %	2.5 wt. %
$Bi_2O_2CO_3$	1.4 wt. %	-
$NiMnO_3$	2.0 wt. %	5.7 wt. %
CeO_2	-	3.4 wt. %
$GdFeO_3$-type	0.5 wt. %	-

Note. Crystal system: cubic; space group *Im*-3 (No. 204); *Z* = 2. Fractional coordinates: R: 2*a* (0, 0, 0), Mn_{SQ}: 6*b* (0, 0.5, 0.5), Ni/Mn: 8*c* (0.25, 0.25, 0.25), and O: 24*g* (*x*, *y*, 0). Occupation factors, *g*, of R, Mn_{SQ}, and O sites are 1. Occupation of Ni/Mn site was fixed at 0.5Ni + 0.5Mn. *R* values are given after background subtraction; *R* values in parenthesis are without background subtraction. For $GdFeO_3$-type impurity in R = Bi, *a* = 5.5767 Å, *b* = 7.7491 Å, and *c* = 5.4052 Å.

The results of the specific heat measurements are given in Figures 2–4. None of the samples showed sharp peaks on specific heat curves. Nevertheless, clear anomalies were observed that could be assigned to long-range magnetic orderings. $BiMn_3Ni_2Mn_2O_{12}$ showed a clear kink at 36 K (Figure 2), below which the C_p/T values started decreasing sharply. High magnetic fields (up to 90 kOe) had almost no effects on the specific heat values of $BiMn_3Ni_2Mn_2O_{12}$, suggesting that the magnetic state was quite robust. $CeMn_3Ni_2Mn_2O_{12}$ showed a broadened kink at 33 K (Figure 3) and a second kink at 27 K, below which the C_p/T values started decreasing. High magnetic fields (up to 90 kOe) had weak effects on the specific heat values of $CeMn_3Ni_2Mn_2O_{12}$, and moved the positions of the broad anomaly to slightly higher temperatures. $HoMn_3Ni_2Mn_2O_{12}$ showed two broadened peaks near 36 K and 10 K (Figure 4). High magnetic fields (up to 90 kOe) noticeably smeared the anomaly near 10 K, and moved the positions of the second broad anomaly to slightly lower temperatures. The specific heat data of $HoMn_3Ni_2Mn_2O_{12}$ were very close to the specific heat curves of $DyMn_3Ni_2Mn_2O_{12}$ [48].

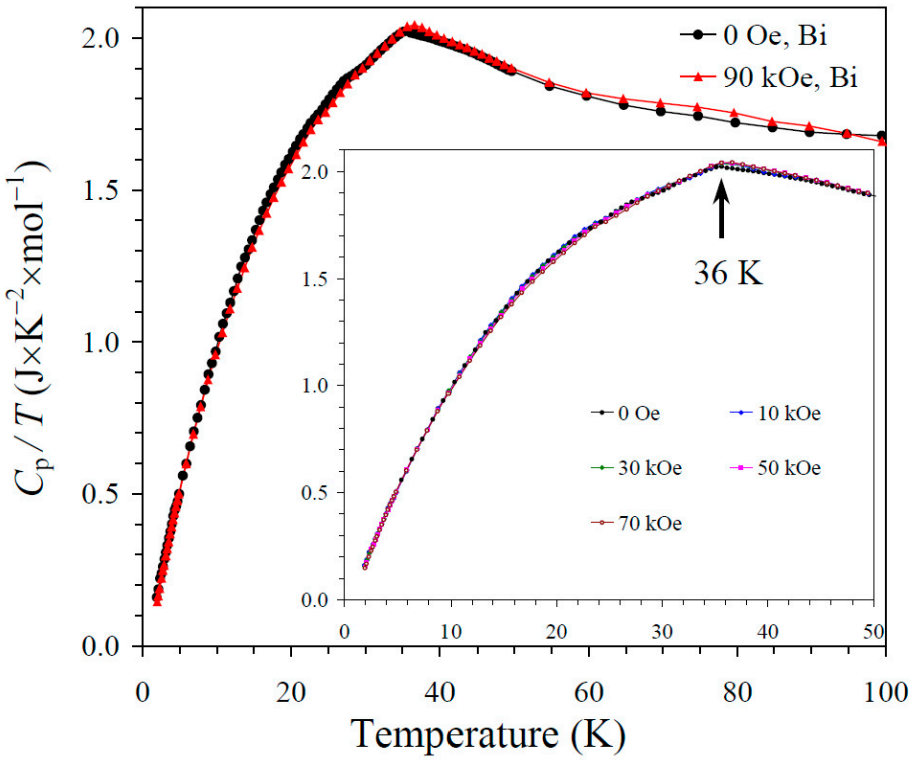

Figure 2. C_p/T versus T curves of $BiMn_3Ni_2Mn_2O_{12}$ measured at H = 0 (black curves) and 90 kOe (red curves). The inset shows C_p/T versus T curves at H = 0, 10, 30, 50, and 70 kOe. The arrow shows the magnetic transition temperature.

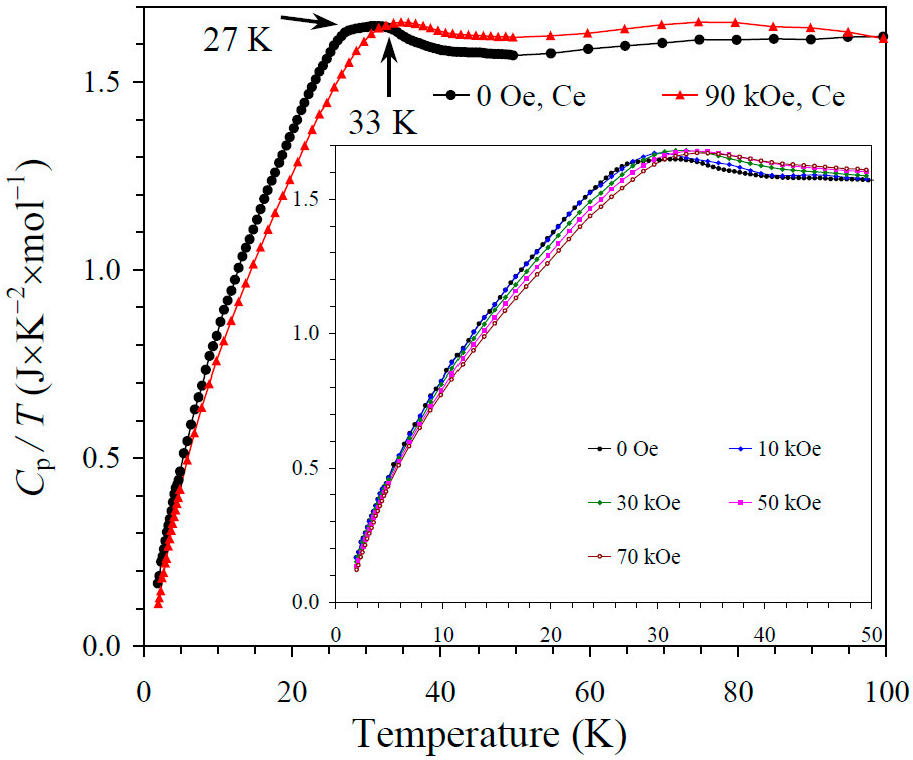

Figure 3. C_p/T versus T curves of $CeMn_3Ni_2Mn_2O_{12}$ measured at H = 0 (black curves) and 90 kOe (red curves). The inset shows C_p/T versus T curves at H = 0, 10, 30, 50, and 70 kOe. The arrows show magnetic transition temperatures.

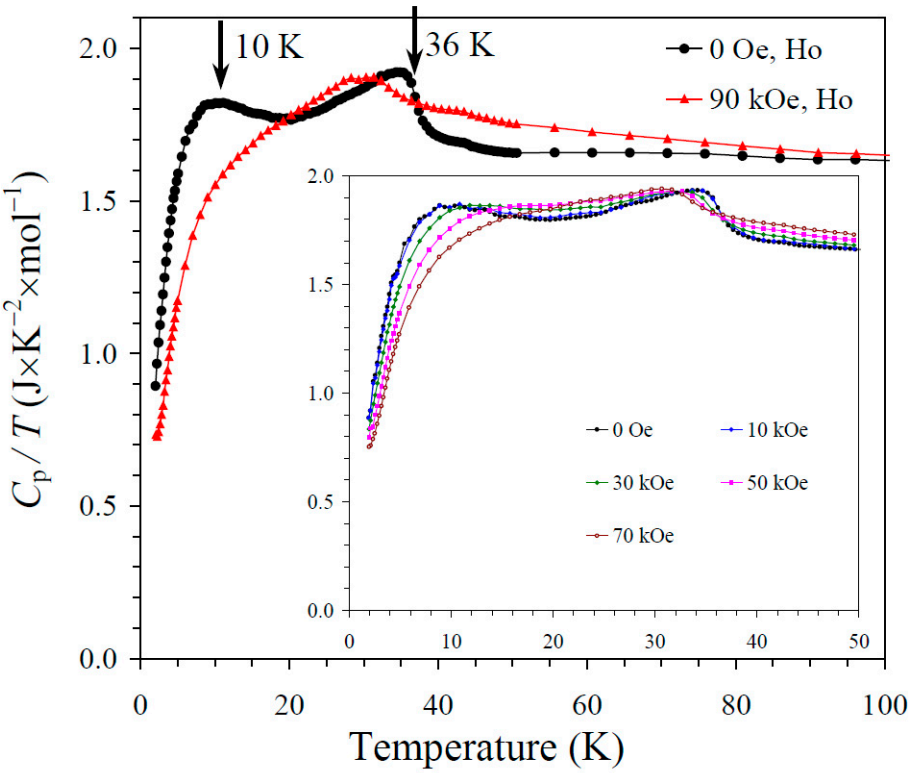

Figure 4. C_p/T versus T curves of $HoMn_3Ni_2Mn_2O_{12}$ measured at H = 0 (black curves) and 90 kOe (red curves). The inset shows C_p/T versus T curves at H = 0, 10, 30, 50, and 70 kOe. The arrows show magnetic transition temperatures.

The temperature dependence of the magnetic susceptibility of $BiMn_3Ni_2Mn_2O_{12}$ is shown in Figure 5a, and Figure 5b gives an M versus H curve at 5 K, 60 K, and 300 K. The divergence between the ZFC and FCC curves was observed below about 15 K at H = 10 kOe; at the same temperature, a broad maximum was observed on the ZFC curve. However, no clear anomalies were detected near 36 K, even on differential curves. Therefore, only specific heat data could clearly identify a magnetic phase transition temperature in $BiMn_3Ni_2Mn_2O_{12}$. The M versus H curves showed a very weak step-like hysteresis near the origin. The hysteresis near the origin probably originated from a small amount of ferrimagnetic $NiMnO_3$ impurity (with T_C = 430 K [66]) with soft ferrimagnetic properties, as the hysteresis was observed even at 300 K. A slim extended hysteresis observed at 5 K (the inset of Figure 5b) originated from $BiMn_3Ni_2Mn_2O_{12}$.

The temperature dependence of the magnetic susceptibility of $CeMn_3Ni_2Mn_2O_{12}$ is shown in Figure 6a, and Figure 6b gives an M versus H curve at 5 K, 60 K, and 300 K. The divergence between the ZFC and FCC curves was observed below about 10 K at H = 10 kOe; at nearly the same temperature, a broad maximum was observed on the ZFC curve. The differential curves showed some anomalies; for example, the $d\chi T/dT$ versus T curves at H = 100 Oe showed peaks at 27 K with shoulders at 33 K, in agreement with the specific heat data; on the other hand, at H = 10 kOe, only one broad anomaly was seen at 33 K. The M versus H curve at 5 K demonstrated a slim extended hysteresis. Above T_N (at 60 K and 300 K), a very weak, step-like hysteresis was observed near the origin, originating from ferrimagnetic $NiMnO_3$ impurity [66]. Therefore, the extended hysteresis at 5 K should originate from the main phase.

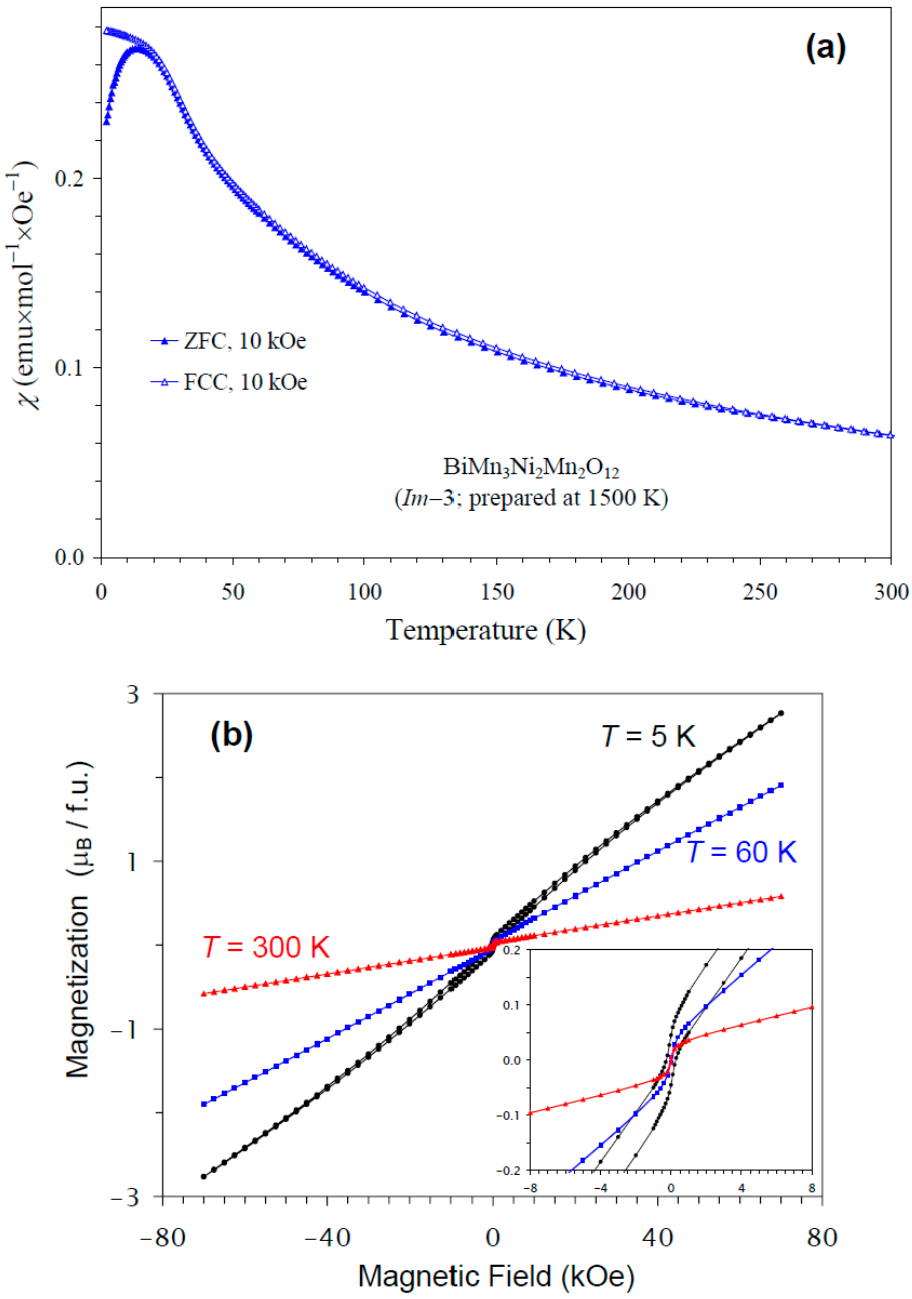

Figure 5. (**a**) ZFC (filled symbols) and FCC (empty symbols) dc magnetic susceptibility curves ($\chi = M/H$) of $BiMn_3Ni_2Mn_2O_{12}$ measured at H = 10 kOe. (**b**) M versus H curves of $BiMn_3Ni_2Mn_2O_{12}$ at T = 5 K, 60 K, and 300 K. The inset shows magnified parts near the origin.

The temperature dependence of the magnetic susceptibility of $HoMn_3Ni_2Mn_2O_{12}$ is shown in Figure 7a, and Figure 7b gives M versus H curves at 5 K and 60 K. In this case, kinks on the χ versus T curves were clearly observed at 36 K. The differential $d\chi/dT$ versus T curves at H = 100 Oe and 10 kOe showed sharp anomalies at 36 K and broader anomalies near 10 K, in agreement with the specific heat data. The M versus H curves showed almost no hysteresis. No detectable step-like hysteresis was observed near the origin at 60 K (above T_N of $HoMn_3Ni_2Mn_2O_{12}$) from $NiMnO_3$ impurity, because of its very small amount. The χ versus T and M versus H curves of $HoMn_3Ni_2Mn_2O_{12}$ were very close to those of $DyMn_3Ni_2Mn_2O_{12}$ [48]. The ground states of Ho^{3+} and Dy^{3+} cations are, of course, different [67]. Nevertheless, these cations are quite close to each other, as they have close ionic radii ($r_{VIII}(Dy^{3+})$ = 1.027 Å versus $r_{VIII}(Ho^{3+})$ = 1.015 Å [65]), effective calculated

magnetic moments (10.63μ_B for Dy^{3+} versus 10.60μ_B for Ho^{3+} [67]), and maximum ordered magnetic moments (of 10μ_B). Therefore, it could be expected that $HoMn_3Ni_2Mn_2O_{12}$ and $DyMn_3Ni_2Mn_2O_{12}$ would have similar magnetic properties and ground states.

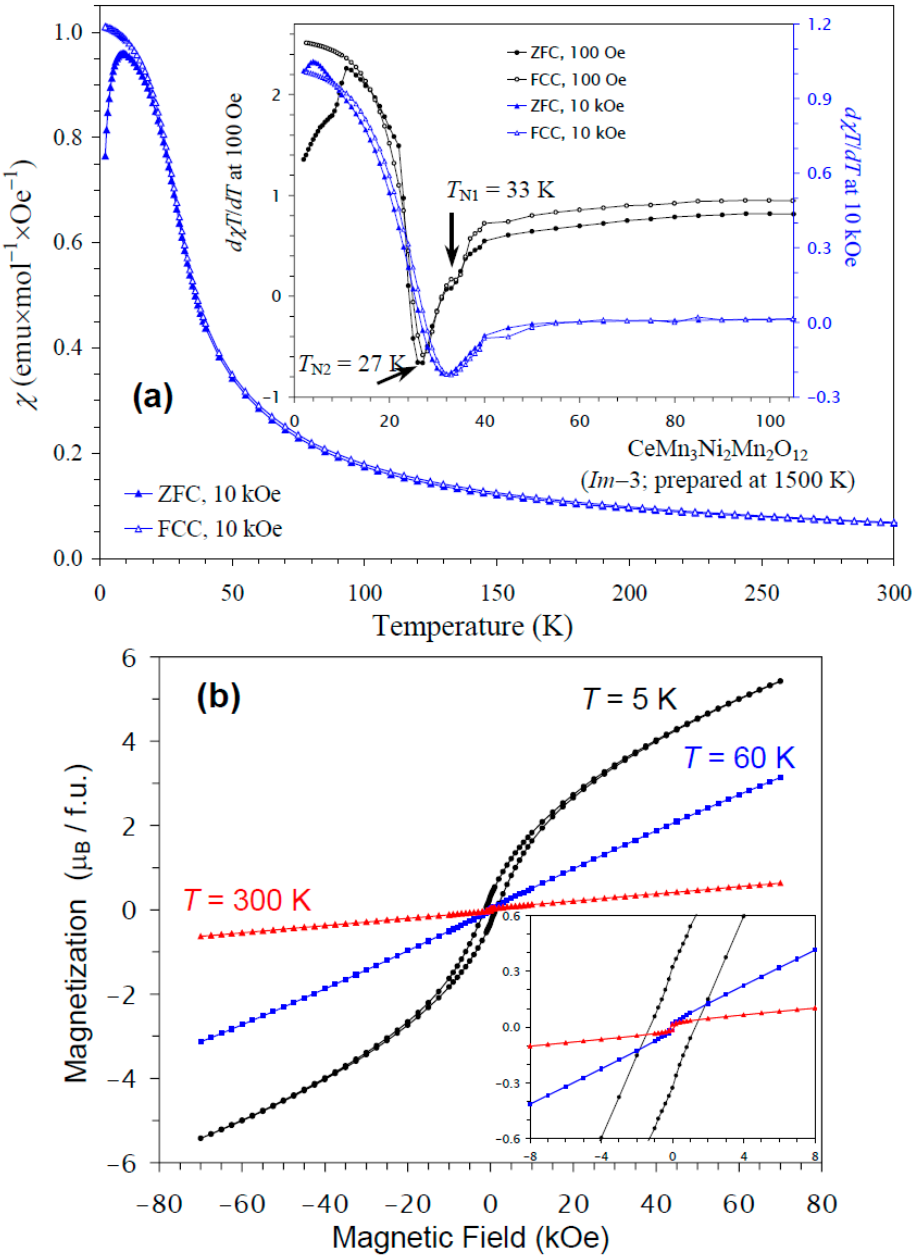

Figure 6. (**a**) ZFC (filled symbols) and FCC (empty symbols) dc magnetic susceptibility curves ($\chi = M/H$) of $CeMn_3Ni_2Mn_2O_{12}$ measured at H = 10 kOe. The inset shows ZFC and FCC dχT/dT versus T curves at H = 100 Oe (black curves) and 10 kOe (blue curves). (**b**) M versus H curves of $CeMn_3Ni_2Mn_2O_{12}$ at T = 5 K, 60 K, and 300 K. The inset shows magnified parts near the origin.

$NiMnO_3$ is a ferrimagnetic material with a T_C of about 430 K [66]. Therefore, it gives noticeable contributions to the measured magnetic properties in small magnetic fields (such as 100 Oe (Figure S2)) below 400 K (Figure 8). As $NiMnO_3$ is a soft ferrimagnetic material, its magnetization saturates at high magnetic fields. Therefore, the larger the measurement magnetic field, the smaller the relative contribution of $NiMnO_3$. However, we found that even at 70 kOe (the maximum available magnetic field), contributions from $NiMnO_3$ affected parameters of the Curie–Weiss fits below 400 K (Figure 8). Therefore, we performed high-temperature magnetic measurements up to 750 K. Above about 440 K, magnetic

susceptibilities were independent of the measurement magnetic field, and reliable, intrinsic Curie–Weiss parameters could be obtained. Inverse magnetic susceptibilities followed the Curie–Weiss law at high temperatures. The Curie–Weiss fits were performed between 480 and 750 K (for the 70 kOe FCC curves), and the resultant parameters are summarized in Table 3. The experimental effective magnetic moments (μ_{eff}) were very close to the calculated values (μ_{calc}), supporting the charges of magnetic cations. In particular, the inclusion of the magnetic moment of Ce^{3+} [67] in the calculation gave a better agreement between μ_{eff} and μ_{calc}; this fact gives indirect support for the +3 oxidation state of Ce, in addition to the structural data. We note that the Curie–Weiss temperatures (θ) were very small for the R = Ce and Ho samples when the fits were performed between 200 K and 380 K at 70 kOe (Figure 8).

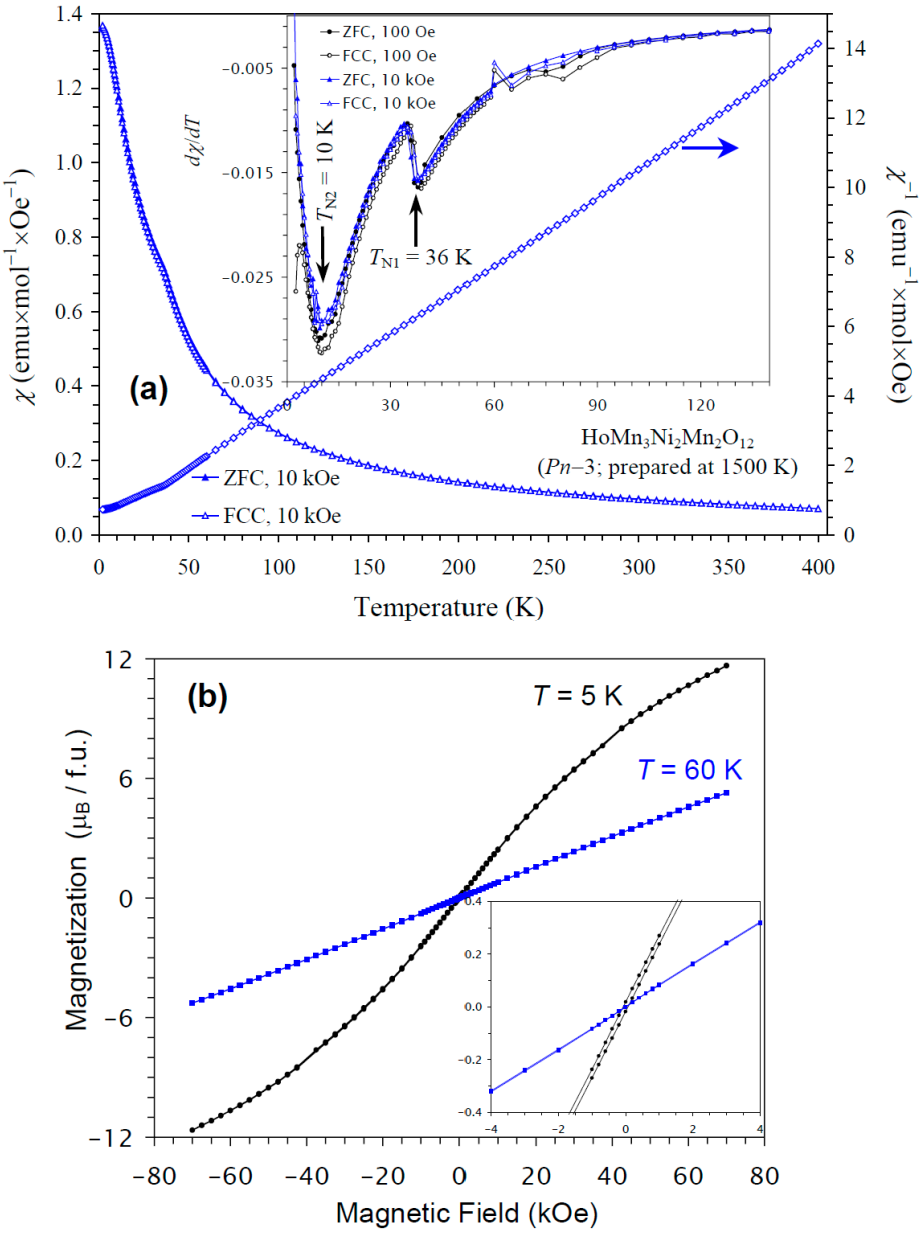

Figure 7. (**a**) ZFC (filled symbols) and FCC (empty symbols) dc magnetic susceptibility curves ($\chi = M/H$) of $HoMn_3Ni_2Mn_2O_{12}$ measured at H = 10 kOe. The inset shows ZFC and FCC $d\chi/dT$ versus T curves at H = 100 Oe (black curves) and 10 kOe (blue curves). The right-hand axis shows the FCC χ^{-1} versus T curve. The arrows show the magnetic transition temperatures. (**b**) M versus H curves of $HoMn_3Ni_2Mn_2O_{12}$ at T = 5 K and 60 K. The inset shows magnified parts near the origin.

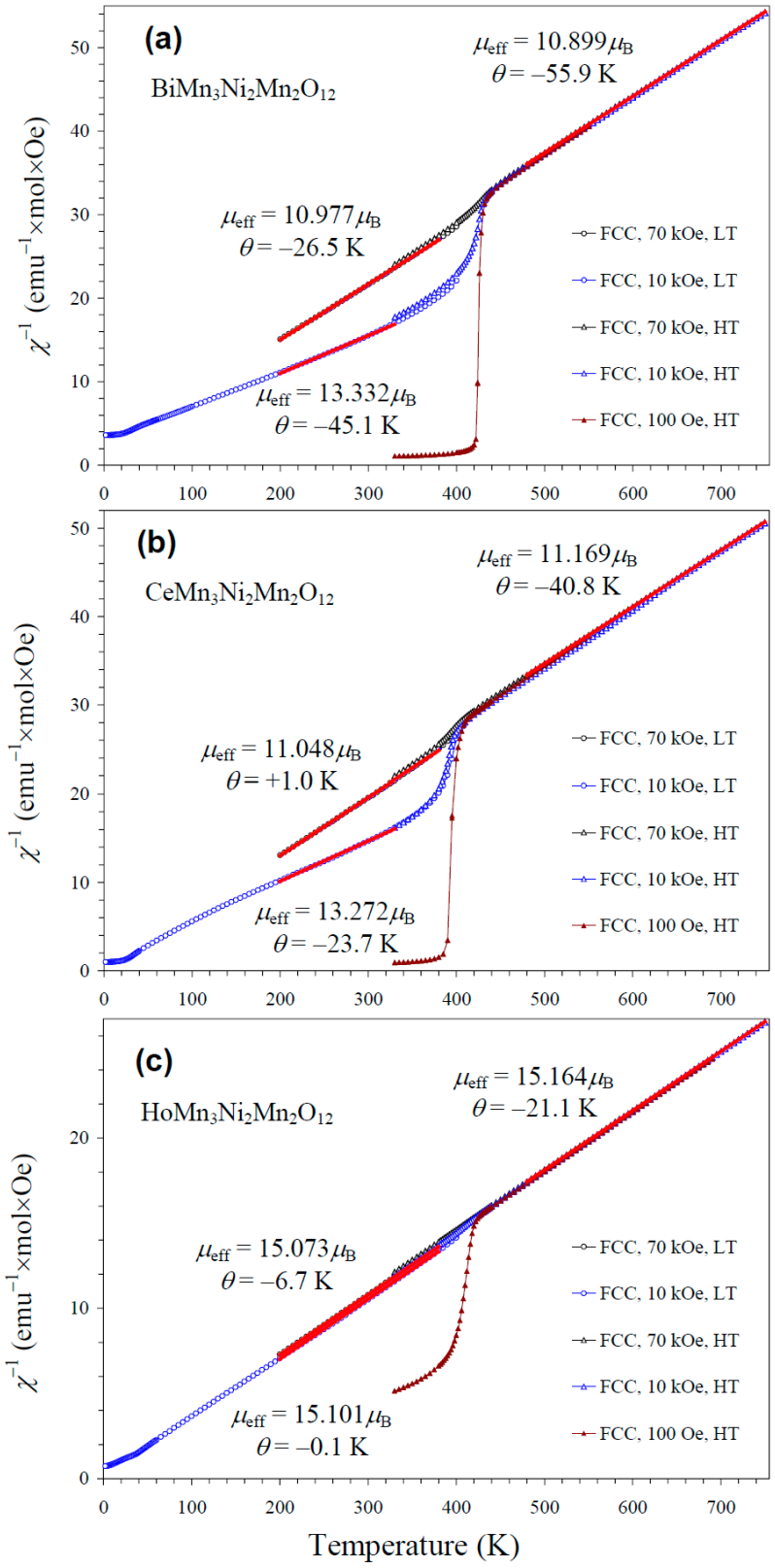

Figure 8. Inverse dc magnetic susceptibility curves ($\chi^{-1} = H/M$) of (**a**) $BiMn_3Ni_2Mn_2O_{12}$, (**b**) $CeMn_3Ni_2Mn_2O_{12}$, and (**c**) $HoMn_3Ni_2Mn_2O_{12}$ measured at H = 100 Oe (brown), 10 kOe (blue), and 70 kOe (black) on cooling (FCC curves) in the low-temperature (LT) region of 2–400 K (circles) and the high-temperature (HT) region of 330–750 K (triangles). The red lines show Curie–Weiss fits (for the 70 kOe data at HT and for the 10 kOe and 70 kOe data at LT); parameters of the fits are given in the figure.

Table 3. Temperatures of magnetic anomalies and parameters of Curie–Weiss fits and M versus H curves at T = 5 K for $RMn_3Ni_2Mn_2O_{12}$.

R (Symmetry)	T_N (K)	μ_{eff} (μ_B/f.u.)	μ_{calc} (μ_B/f.u.)	θ (K)	M_S (μ_B/f.u.)
Bi (*Im*-3)	36	10.899(2)	10.863	−55.9(3)	2.76
Ce (*Im*-3)	27, 33	11.169(1)	11.125	−40.8(2)	5.42
Ho (*Pn*-3)	10, 36	15.164(2)	15.178	−21.1(1)	11.66

The Curie–Weiss fits were performed between 480 K and 750 K using the FCC χ^{-1} versus T data at 70 kOe. M_S is the magnetization value at T = 5 K and H = 70 kOe. μ_{calc} was calculated using 2.4μ_B for Ce^{3+}, 10.6μ_B for Ho^{3+}, 4.899μ_B for Mn^{3+}, 2.828μ_B for Ni^{2+}, and 3.873μ_B for Mn^{4+} [67]. T_N values were determined from peaks on the 100 Oe and 10 kOe FCC $d(\chi T)/dT$ versus T or $d\chi/dT$ versus T curves, or from specific heat data.

$RMn_3Ni_2Mn_2O_{12}$ samples with R = Bi, Ce, and Ho were prepared under the same synthesis conditions (6 GPa and 1500 K). The same synthesis conditions were used for the preparation of $RMn_3Ni_2Mn_2O_{12}$ with R = Nd, Sm, Gd, and Dy [48]. These conditions produced partial ordering of Ni^{2+} and Mn^{4+} cations in the case of R = Nd-Ho. It was also found that an increase in the synthesis temperature to 1700 K produced samples with a disordered arrangement of Ni^{2+} and Mn^{4+} cations in the case of R = Nd and Sm [48]. Therefore, the disordered arrangement of Ni^{2+} and Mn^{4+} cations found in the R = Bi and Ce samples prepared at 1500 K could suggest that a (partial) ordering may be realized at lower synthesis temperatures. This possibility may be explored in the future. Note that larger amounts of impurities in the R = Ce sample (Table 2) could shift the real chemical composition of the main phase and contribute to the stabilization of the disordered structure.

3. Experimental

$RMn_3Ni_2Mn_2O_{12}$ samples with R = Bi, Ce, and Ho were prepared from stoichiometric mixtures of Bi_2O_3 (Rare Metallic Co., Tokyo, Japan, 99.9999%), CeO_2 (Rare Metallic Co., Tokyo, Japan, 99.99%), Ho_2O_3 (Rare Metallic Co., Tokyo, Japan, 99.9%), Mn_2O_3 (Rare Metallic Co., Tokyo, Japan, 99.99%), MnO_2 (Alfa Aesar, Ward Hill, MA, USA, 99.99%), and NiO (Rare Metallic Co., Tokyo, Japan, 99.9%). Single-phase Mn_2O_3 was prepared from a commercial MnO_2 chemical (Rare Metallic Co., Tokyo, Japan, 99.99%) by annealing in air at 923 K for 24 h. The synthesis was performed at about 6 GPa and at about 1500 K for 2 h in sealed Au capsules, using a belt-type HP instrument. After annealing at 1500 K, the samples were cooled down to room temperature by turning off the heating current, and the pressure was slowly released.

X-ray powder diffraction (XRPD) data were collected at room temperature on a MiniFlex600 diffractometer (Rigaku, Tokyo, Japan) using CuKα radiation (2θ range of 8–100°, step width of 0.02°, and scan speed of 2°/min). Room-temperature synchrotron XRPD data were measured using the beamline BL02B2 [68,69] of SPring-8, Japan. Intensity data were collected between 1.00° and 83.02° at a 0.006° interval in 2θ with 100 s exposure time. A wavelength of λ = 0.4137875 Å was used for R = Bi (to reduce the absorption effect because of the presence of heavy Bi). A wavelength of λ = 0.6200666 Å was used for R = Ce and Ho. The samples were placed into open Lindemann glass capillary tubes (inner diameter: 0.2 mm), which were rotated during measurements. The Rietveld analysis of all XRPD data was performed using the *RIETAN-2000* program [70]. Normalized (because of different measurement times) background (obtained through measurements of (different) empty capillary tubes) was subtracted from the raw synchrotron XRPD data. Background subtraction usually gives larger profile agreement factors (R_{wp} and R_p) because background intensities become very low. On the other hand, the background subtraction usually improves integrated agreement factors (R_I and R_F) because better structure descriptions are achieved. The remaining background was fitted by 12-order Legendre polynomials. We

note that $NiMnO_3$ impurity was fitted using the ilmenite-type model (space group *R*-3) in the R = Bi and Ce samples, and using the simple corundum-type model (space group *R*-3*c*) in the R = Ho sample, because of its very small amount.

Magnetic measurements were performed on SQUID magnetometers (Quantum Design MPMS3, San Diego, CA, USA) between 2 and 400 K in applied fields of 100 Oe, 10 kOe, and 70 kOe, under both zero-field-cooled (ZFC) and field-cooled on cooling (FCC) conditions. High-temperature magnetic measurements were performed between 330 K and 750 K with the same magnetic fields using a high-temperature MPMS3 option, where dense pellets of the samples with polished flat surfaces were attached to a high-temperature stick with Zircar cement. Isothermal magnetization was measured at temperatures of 5 K, 60 K, and 300 K, between −70 and 70 kOe.

The specific heat, C_p, was measured on cooling from 100 K to 2 K at different magnetic fields up to 90 kOe by a pulse relaxation method, using a commercial calorimeter (Quantum Design PPMS, San Diego, CA, USA). All magnetic and specific heat measurements were performed using pieces of dense pellets.

4. Conclusions

The synthesis of A site-ordered quadruple perovskites, $RMn_3Ni_2Mn_2O_{12}$ with R = Bi, Ce, and Ho, was performed by a high-pressure, high-temperature method at about 6 GPa and about 1500 K. Despite using the same synthesis conditions, the R = Bi and Ce samples crystallized in space group *Im*-3 with a disordered arrangement of Ni^{2+} and Mn^{4+} cations. On the other hand, the R = Ho sample crystallized in space group *Pn*-3 with partial ordering of Ni^{2+} and Mn^{4+} cations. By using a combination of magnetic susceptibility and specific heat measurements, one magnetic transition was detected in the R = Bi sample near 36 K. On the other hand, two magnetic transitions were found near 27 K and 33 K in the R = Ce sample, and near 10 K and 36 K in the R = Ho sample. Magnetic properties were affected by the presence of ferrimagnetic $NiMnO_3$ impurity (with a T_C of about 430 K). Therefore, Curie–Weiss parameters were estimated for all samples from high-temperature magnetic measurements up to 750 K. The total effective magnetic moment for R = Ce and structural information, obtained from the state-of-the-art synchrotron X-ray powder diffraction, suggested the presence of Ce^{3+}.

Supplementary Materials: The following supporting information can be downloaded at https://www.mdpi.com/article/10.3390/molecules30081749/s1: Figure S1: Fragments (between 3° and 25°) and magnified parts of experimental, calculated, and difference synchrotron X-ray powder diffraction patterns of $BiMn_3Ni_2Mn_2O_{12}$ at T = 297 K; Figure S2: ZFC and FCC magnetic susceptibility curves of $RMn_3Ni_2Mn_2O_{12}$ with R = Bi, Ce, and Ho at H = 100 Oe, between 330 K and 550 K.

Funding: This research received no external funding.

Institutional Review Board Statement: Not applicable.

Informed Consent Statement: Not applicable.

Data Availability Statement: The raw data supporting the conclusions of this article will be made available by the author upon request.

Acknowledgments: Synchrotron radiation experiments were conducted on the powder diffraction beamline BL02B2 at SPring-8, with the permission from the Japan Synchrotron Radiation Research Institute (Proposal Number: 2024B1825). The author thanks Y. Mori for his help with BL02B2 of SPring-8, and R. Liu for her preliminary studies of $RMn_3Ni_2Mn_2O_{12}$ compounds. MANA was supported by the World Premier International Research Center Initiative (WPI), MEXT, Japan.

Conflicts of Interest: The author declares no conflicts of interest.

References

1. Mitchell, R.H. *Perovskites: Modern and Ancient*; Almaz Press: Thunder Bay, ON, Canada, 2002.
2. Abakumov, A.M.; Tsirlin, A.A.; Antipov, E.V. Transition-metal perovskites. In *Comprehensive Inorganic Chemistry II (Second Edition): From Elements to Applications*; Reedijk, J., Poeppelmeier, K.R., Eds.; Elsevier: Amsterdam, The Netherlands, 2013; Volume 2, pp. 1–40.
3. Knapp, M.C.; Woodward, P.M. A-site cation ordering in $AA'BB'O_6$ perovskites. *J. Solid State Chem.* **2006**, *179*, 1076–1085. [CrossRef]
4. King, G.; Woodward, P.M. Cation ordering in perovskites. *J. Mater. Chem.* **2010**, *20*, 5785–5796. [CrossRef]
5. Vasala, S.; Karppinen, M. $A_2B'B''O_6$ perovskites: A review. *Prog. Solid State Chem.* **2015**, *43*, 1–36. [CrossRef]
6. Bousquet, E.; Cano, A. Non-collinear magnetism in multiferroic perovskites. *J. Phys. Condens. Matter* **2016**, *28*, 123001. [CrossRef]
7. Vasil'ev, A.N.; Volkova, O.S. New functional materials $AC_3B_4O_{12}$ (Review). *Low Temp. Phys.* **2007**, *33*, 895–914. [CrossRef]
8. Long, Y. A-site ordered quadruple perovskite oxides $AA'_3B_4O_{12}$. *Chin. Phys. B* **2016**, *25*, 078108. [CrossRef]
9. Yamada, I. Novel catalytic properties of quadruple perovskites. *Sci. Technol. Adv. Mater.* **2017**, *18*, 541–548. [CrossRef] [PubMed]
10. Belik, A.A.; Johnson, R.D.; Khalyavin, D.D. The rich physics of A-site-ordered quadruple perovskite manganites AMn_7O_{12}. *Dalton Trans.* **2021**, *50*, 15458–15472. [CrossRef]
11. Ding, J.; Zhu, X.H. Research progress on quadruple perovskite oxides. *J. Mater. Chem. C* **2024**, *12*, 9510–9561. [CrossRef]
12. Yin, Y.Y.; Liu, M.; Dai, J.H.; Wang, X.; Zhou, L.; Cao, H.; Cruz, C.D.; Chen, C.T.; Xu, Y.; Shen, X.; et al. $LaMn_3Ni_2Mn_2O_{12}$: An A- and B-site ordered quadruple perovskite with A-site tuning orthogonal spin ordering. *Chem. Mater.* **2016**, *28*, 8988–8996. [CrossRef]
13. Liu, M.; Hu, C.E.; Cheng, C.; Chen, X.R. A–B-intersite-dependent magnetic order and electronic structure of $LaMn_3Ni_2Mn_2O_{12}$: A first-principles study. *J. Phys. Chem. C* **2018**, *122*, 1946–1954. [CrossRef]
14. Byeon, S.H.; Lufaso, M.W.; Parise, J.B.; Woodward, P.M.; Hansen, T. High-pressure synthesis and characterization of perovskites with simultaneous ordering of both the A- and B-site cations, $CaCu_3Ga_2M_2O_{12}$ (M = Sb, Ta). *Chem. Mater.* **2003**, *15*, 3798–3804. [CrossRef]
15. Byeon, S.H.; Lee, S.S.; Parise, J.B.; Woodward, P.M.; Hur, N.H. High-pressure synthesis of metallic perovskite ruthenate $CaCu_3Ga_2Ru_2O_{12}$. *Chem. Mater.* **2004**, *16*, 3697–3701. [CrossRef]
16. Byeon, S.H.; Lee, S.S.; Parise, J.B.; Woodward, P.M.; Hur, N.H. New ferrimagnetic oxide $CaCu_3Cr_2Sb_2O_{12}$: High-pressure synthesis, structure, and magnetic properties. *Chem. Mater.* **2005**, *17*, 3552–3557. [CrossRef]
17. Deng, H.S.; Liu, M.; Dai, J.H.; Hu, Z.W.; Kuo, C.Y.; Yin, Y.Y.; Yang, J.Y.; Wang, X.; Zhao, Q.; Xu, Y.; et al. Strong enhancement of spin ordering by A-site magnetic ions in the ferrimagnet $CaCu_3Fe_2Os_2O_{12}$. *Phys. Rev. B* **2016**, *94*, 024414. [CrossRef]
18. Wang, X.; Liu, Z.; Deng, H.; Agrestini, S.; Chen, K.; Lee, J.F.; Lin, H.J.; Chen, C.T.; Choueikani, F.; Ohresser, P.; et al. Comparative study on the magnetic and transport properties of B-site ordered and disordered $CaCu_3Fe_2Os_2O_{12}$. *Inorg. Chem.* **2022**, *61*, 16929–16935. [CrossRef]
19. Wang, X.; Liu, M.; Shen, X.D.; Liu, Z.H.; Hu, Z.W.; Chen, K.; Ohresser, P.; Nataf, L.; Baudelet, F.; Lin, H.J.; et al. High-temperature ferrimagnetic half metallicity with wide spin-up energy gap in $NaCu_3Fe_2Os_2O_{12}$. *Inorg. Chem.* **2019**, *58*, 320–326. [CrossRef]
20. Ye, X.; Liu, Z.; Wang, W.; Hu, Z.; Lin, H.J.; Weng, S.C.; Chen, C.T.; Yu, R.; Tjeng, L.H.; Long, Y.W. High-pressure synthesis and spin glass behavior of a Mn/Ir disordered quadruple perovskite $CaCu_3Mn_2Ir_2O_{12}$. *J. Phys. Condens. Matter* **2020**, *32*, 075701. [CrossRef]
21. Li, H.P.; Zhang, Q.; Zhu, Z.P.; Ge, Z.Z.; Li, C.S.; Meng, J.; Tian, Y. Unraveling the effect of B-site antisite defects on the electronic and magnetic properties of the quadruple perovskite $CaCu_3Fe_2Nb_2O_{12}$. *Phys. Chem. Chem. Phys.* **2019**, *21*, 3059–3065. [CrossRef]
22. Guo, J.; Shen, X.D.; Liu, Z.H.; Qin, S.J.; Wang, W.P.; Ye, X.B.; Liu, G.X.; Yu, R.C.; Lin, H.J.; Chen, C.T.; et al. High-pressure synthesis of a B-site Co^{2+}/Mn^{4+} disordered quadruple perovskite $LaMn_3Co_2Mn_2O_{12}$. *Inorg. Chem.* **2020**, *59*, 12445–12452. [CrossRef]
23. Liu, Z.; Sun, Q.; Ye, X.; Wang, X.; Zhou, L.; Shen, X.; Chen, K.; Nataf, L.; Baudelet, F.; Agrestini, S.; et al. Quadruple perovskite oxide $LaCu_3Co_2Re_2O_{12}$: A ferrimagnetic half metal with nearly 100% B-site degree of order. *Appl. Phys. Lett.* **2020**, *117*, 152402. [CrossRef]
24. Li, S.M.; Shu, M.F.; Wang, M.; Pan, C.B.; Zhao, G.C.; Yin, L.H.; Song, W.H.; Yang, J.; Zhu, X.B.; Sun, Y.P. Critical behavior at paramagnetic to ferrimagnetic phase transition in A-site ordered perovskite $CaCu_3Cr_2Nb_2O_{12}$. *Phys. B Condens. Matter* **2023**, *648*, 414376. [CrossRef]
25. Morimura, A.; Kamiyama, S.; Hayashi, N.; Yamamoto, H.; Yamada, I. High-pressure syntheses, crystal structures, and magnetic properties of novel quadruple perovskite oxides $LaMn_3Ru_2Mn_2O_{12}$ and $LaMn_3Ru_2Fe_2O_{12}$. *J. Alloys Compd.* **2023**, *968*, 172263. [CrossRef]
26. Zhang, J.; Liu, Z.H.; Ye, X.B.; Wang, X.; Lu, D.B.; Zhao, H.T.; Pi, M.C.; Chen, C.T.; Chen, J.L.; Kuo, C.Y.; et al. High-pressure synthesis of quadruple perovskite oxide $CaCu_3Cr_2Re_2O_{12}$ with a high ferrimagnetic Curie temperature. *Inorg. Chem.* **2024**, *63*, 3499–3505. [CrossRef]

27. Kumar, L.; Datta, J.; Sen, S.; Ray, P.P.; Mandal, T.K. Ambient pressure synthesis and properties of $LaCu_3Fe_2TiSbO_{12}$: New A-site ordered ferrimagnetic quadruple perovskite. *J. Solid State Chem.* **2021**, *302*, 122433. [CrossRef]
28. Kumar, L.; Sen, S.; Mandal, T.K. Ambient pressure synthesis and structure and magnetic properties of a new A- and B-site ordered multinary quadruple perovskite. *Dalton Trans.* **2024**, *53*, 11060–11070. [CrossRef]
29. Dass, R.I.; Yan, J.Q.; Goodenough, J.B. Oxygen stoichiometry, ferromagnetism, and transport properties of $La_{2-x}NiMnO_{6+\delta}$. *Phys. Rev. B* **2003**, *68*, 064415. [CrossRef]
30. Rogado, N.S.; Li, J.; Sleight, A.W.; Subramanian, M.A. Magnetocapacitance and magnetoresistance near room temperature in a ferromagnetic semiconductor: La_2NiMnO_6. *Adv. Mater.* **2005**, *17*, 2225–2227. [CrossRef]
31. Kobayashi, Y.; Shiozawa, M.; Sato, K.; Abe, K.; Asai, K. Crystal structure, magnetism, and dielectric properties of $La_{1-x}Bi_xNi_{0.5}Mn_{0.5}O_3$. *J. Phys. Soc. Jpn.* **2008**, *77*, 084701. [CrossRef]
32. Choudhury, D.; Mandal, P.; Mathieu, R.; Hazarika, A.; Rajan, S.; Sundaresan, A.; Waghmare, U.V.; Knut, R.; Karis, O.; Nordblad, P.; et al. Near-room-temperature colossal magnetodielectricity and multiglass properties in partially disordered La_2NiMnO_6. *Phys. Rev. Lett.* **2012**, *108*, 127201. [CrossRef]
33. Guo, Y.Q.; Shi, L.; Zhou, S.M.; Zhao, J.I.; Liu, W.J. Near room-temperature magnetoresistance effect in double perovskite La_2NiMnO_6. *Appl. Phys. Lett.* **2013**, *102*, 222401. [CrossRef]
34. Sánchez-Benítez, J.; Martínez-Lope, M.J.; Alonso, J.A.; García-Muñoz, J.L. Magnetic and structural features of the $NdNi_{1-x}Mn_xO_3$ perovskite series investigated by neutron diffraction. *J. Phys. Condens. Matter* **2011**, *23*, 226001. [CrossRef]
35. Retuerto, M.; Muñoz, Á.; Martínez-Lope, M.J.; Alonso, J.A.; Mompeán, F.J.; Fernández-Díaz, M.T.; Sánchez-Benítez, J. Magnetic interactions in the double perovskites R_2NiMnO_6 (R = Tb, Ho, Er, Tm) investigated by neutron diffraction. *Inorg. Chem.* **2015**, *54*, 10890–10900. [CrossRef] [PubMed]
36. Booth, R.J.; Fillman, R.; Whitaker, H.; Nag, A.; Tiwari, R.M.; Ramanujachary, K.V.; Gopalakrishnan, J.; Lofland, S.E. An investigation of structural, magnetic and dielectric properties of R_2NiMnO_6 (R = rare earth, Y). *Mater. Res. Bull.* **2009**, *44*, 1559–1564. [CrossRef]
37. Nasir, M.; Kumar, S.; Patra, N.; Bhattacharya, D.; Jha, S.N.; Basaula, D.R.; Bhatt, S.; Khan, M.; Liu, S.W.; Biring, S.; et al. Role of antisite disorder, rare-earth size, and superexchange angle on band gap, Curie temperature, and magnetization of R_2NiMnO_6 double perovskites. *ACS Appl. Electron. Mater.* **2019**, *1*, 141–153. [CrossRef]
38. Asai, K.; Fujiyoshi, K.; Nishimori, N.; Satoh, Y.; Kobayashi, Y.; Mizoguchi, M. Magnetic properties of $REMe_{0.5}Mn_{0.5}O_3$ (RE = rare earth element, Me = Ni, Co). *J. Phys. Soc. Jpn.* **1998**, *67*, 4218–4228. [CrossRef]
39. Yi, W.; Liang, Q.F.; Matsushita, Y.; Tanaka, M.; Belik, A.A. High-pressure synthesis, crystal structure, and properties of In_2NiMnO_6 with antiferromagnetic order and field-induced phase transition. *Inorg. Chem.* **2013**, *52*, 14108–14115. [CrossRef]
40. Terada, N.; Khalyavin, D.D.; Manuel, P.; Yi, W.; Suzuki, H.S.; Tsujii, N.; Imanaka, Y.; Belik, A.A. Ferroelectricity induced by ferriaxial crystal rotation and spin helicity in a B-site-ordered double-perovskite multiferroic In_2NiMnO_6. *Phys. Rev. B* **2015**, *91*, 104413. [CrossRef]
41. Yi, W.; Princep, A.J.; Guo, Y.F.; Johnson, R.D.; Khalyavin, D.D.; Manuel, P.; Senyshyn, A.; Presniakov, I.A.; Sobolev, A.V.; Matsushita, Y.; et al. Sc_2NiMnO_6: A double-perovskite with a magnetodielectric response driven by multiple magnetic orders. *Inorg. Chem.* **2015**, *54*, 8012–8021. [CrossRef]
42. Ding, L.; Khalyavin, D.D.; Manuel, P.; Blake, J.; Orlandi, F.; Yi, W.; Belik, A.A. Colossal magnetoresistance in the insulating ferromagnetic double perovskites Tl_2NiMnO_6: A neutron diffraction study. *Acta Mater.* **2019**, *173*, 20–26. [CrossRef]
43. Sobolev, A.V.; Glazkova, I.S.; Akulenko, A.A.; Sergueev, I.; Chumakov, A.I.; Yi, W.; Belik, A.A.; Presniakov, I.A. ^{61}Ni nuclear forward scattering study of magnetic hyperfine interactions in double perovskites A_2NiMnO_6 (A = Sc, In, Tl). *J. Phys. Chem.* **2019**, *123*, 23628–23634. [CrossRef]
44. Terada, N.; Colin, C.V.; Qureshi, N.; Hansen, T.; Matsubayashi, K.; Uwatoko, Y.; Belik, A.A. Pressure-induced incommensurate antiferromagnetic order in a ferromagnetic B-site ordered double-perovskite Lu_2NiMnO_6. *Phys. Rev. B* **2020**, *102*, 094412. [CrossRef]
45. Manna, K.; Bera, A.K.; Jain, M.; Elizabeth, S.; Yusuf, S.M.; Anil Kumar, P.S. Structural-modulation-driven spin canting and reentrant glassy magnetic phase in ferromagnetic Lu_2MnNiO_6. *Phys. Rev. B* **2015**, *91*, 224420. [CrossRef]
46. Dieguez, O.; Iniguez, J. Multiferroic Bi_2NiMnO_6 thin films: A computational prediction. *Phys. Rev. B* **2017**, *95*, 085129. [CrossRef]
47. Weihe, H.; Gudel, H.U. Quantitative interpretation of the Goodenough-Kanamori rules: A critical analysis. *Inorg. Chem.* **1997**, *36*, 3632–3639. [CrossRef]
48. Belik, A.A.; Liu, R.; Tanaka, M.; Yamaura, K. B-site-ordered and disordered structures in A-site-ordered quadruple perovskites $RMn_3Ni_2Mn_2O_{12}$ with R = Nd, Sm, Gd, and Dy. *Molecules* **2024**, *29*, 5488. [CrossRef] [PubMed]
49. Zhou, L.; Dai, J.H.; Chai, Y.S.; Zhang, H.M.; Dong, S.; Cao, H.B.; Calder, S.; Yin, Y.Y.; Wang, X.; Shen, X.D.; et al. Realization of Large Electric Polarization and Strong Magnetoelectric Coupling in $BiMn_3Cr_4O_{12}$. *Adv. Mater.* **2017**, *29*, 1703435. [CrossRef]
50. Maia, A.; Kadlec, C.; Savinov, M.; Vilarinho, R.; Moreira, J.A.; Bovtun, V.; Kempa, M.; Míšek, M.; Kaštil, J.; Prokhorov, A.; et al. Can the Ferroelectric Soft Mode Trigger an Antiferromagnetic Phase Transition? *J. Eur. Ceram. Soc.* **2023**, *43*, 2479–2487. [CrossRef]

51. Etter, M.; Isobe, M.; Sakurai, H.; Yaresko, A.; Dinnebier, R.E.; Takagi, H. Charge disproportionation of mixed-valent Cr triggered by Bi lone-pair effect in the A-site-ordered perovskite $BiCu_3Cr_4O_{12}$. *Phys. Rev. B* **2018**, *97*, 195111. [CrossRef]
52. Khalyavin, D.D.; Johnson, R.D.; Orlandi, F.; Radaelli, P.G.; Manuel, P.; Belik, A.A. Emergent helical texture of electric dipoles. *Science* **2020**, *369*, 680–684. [CrossRef]
53. Belik, A.A.; Matsushita, Y.; Tanaka, M.; Johnson, R.D.; Khalyavin, D.D. A plethora of structural transitions, distortions and modulations in Cu-doped $BiMn_7O_{12}$ quadruple perovskites. *J. Mater. Chem. C* **2021**, *9*, 10232–10242. [CrossRef]
54. Fu, W.T.; Ijdo, D.J.W. "Unusual" phase transitions in $CeAlO_3$. *J. Solid State Chem.* **2006**, *179*, 2732–2738. [CrossRef]
55. Vasylechko, L.; Senyshyna, A.; Trots, D.; Niewa, R.; Schnelle, W.; Knapp, M. $CeAlO_3$ and $Ce_{1-x}R_xAlO_3$ (R = La, Nd) solid solutions: Crystal structure, thermal expansion and phase transitions. *J. Solid State Chem.* **2007**, *180*, 1277–1290. [CrossRef]
56. Errandonea, D.; Santamaria-Perez, D.; Martinez-Garcia, D.; Gomis, O.; Shukla, R.; Achary, S.N.; Tyagi, A.K.; Popescu, C. Pressure impact on the stability and distortion of the crystal structure of $CeScO_3$. *Inorg. Chem.* **2017**, *56*, 8363–8371. [CrossRef]
57. Cao, Y.M.; Cao, S.X.; Ren, W.; Feng, Z.J.; Yuan, S.J.; Kang, B.J.; Lu, B.; Zhang, J.C. Magnetization switching of rare earth orthochromite $CeCrO_3$. *Appl. Phys. Lett.* **2014**, *104*, 232405. [CrossRef]
58. Yuan, S.J.; Cao, Y.M.; Li, L.; Qi, T.F.; Cao, S.X.; Zhang, J.C.; DeLong, L.E.; Cao, G. First-order spin reorientation transition and specific-heat anomaly in $CeFeO_3$. *J. Appl. Phys.* **2013**, *114*, 113909. [CrossRef]
59. Yamada, I.; Etani, H.; Murakami, M.; Hayashi, N.; Kawakami, T.; Mizumaki, M.; Ueda, S.; Abe, H.; Liss, K.D.; Studer, A.J.; et al. Charge-order melting in charge-disproportionated perovskite $CeCu_3Fe_4O_{12}$. *Inorg. Chem.* **2014**, *53*, 11794–11801. [CrossRef] [PubMed]
60. Sánchez-Benítez, J.; Martínez-Lope, M.J.; Alonso, J.A. Preparation at moderate pressures, crystal and magnetic structure and magnetotransport of the ferrimagnetic $CeCu_3Mn_4O_{12}$ perovskite. *J. Appl. Phys.* **2010**, *107*, 103904. [CrossRef]
61. Kadyrova, N.I.; Zainulin, Y.G.; Tyutyunnik, A.P.; Kellerman, D.G.; Mel'nikova, N.V. Preparation specifics and properties of $AMn_3V_4O_{12}$ (A = Ca, Ce, and Sm) high-pressure phases. *Russ. J. Inorg. Chem.* **2017**, *62*, 103–110. [CrossRef]
62. Belik, A.A.; Katsuya, Y.; Tanaka, M.; Yamaura, K. Crystal structure and magnetic properties of A-site-ordered quadruple perovskite $CeCu_3Cr_4O_{12}$. *J. Alloys Compd.* **2019**, *793*, 42–48. [CrossRef]
63. Brese, N.E.; O'Keeffe, M. Bond-valence parameters for solids. *Acta Crystallogr. Sect. B Struct. Sci.* **1991**, *47*, 192–197. [CrossRef]
64. Roulhac, P.L.; Palenik, G.J. Bond valence sums in coordination chemistry. The calculation of the oxidation state of cerium in complexes containing cerium bonded only to oxygen. *Inorg. Chem.* **2003**, *42*, 118–121. [CrossRef] [PubMed]
65. Shannon, R.D. Revised effective ionic radii and systematic studies of interatomic distances in halides and chalcogenides. *Acta Crystallogr. Sect. A Cryst. Phys. Diffr. Theor. Gen. Crystallogr.* **1976**, *32*, 751–767. [CrossRef]
66. Pernet, M.; Joubert, J.C.; Ferrand, B. Etude par diffraction neutronique de l'ilmenite ferrimagnetique $NiMnO_3$. *Solid State Commun.* **1975**, *16*, 503–508. [CrossRef]
67. Kittel, C.; McEuen, P. *Introduction to Solid State Physics*; John Wiley & Sons, Inc.: New York, NY, USA, 2005.
68. Kawaguchi, S.; Takemoto, M.; Osaka, K.; Nishibori, E.; Moriyoshi, C.; Kubota, Y.; Kuroiwa, Y.; Sugimoto, K. High-throughput powder diffraction measurement system consisting of multiple MYTHEN detectors at beamline BL02B2 of SPring-8. *Rev. Sci. Instrum.* **2017**, *88*, 085111. [CrossRef]
69. Kawaguchi, S.; Takemoto, M.; Tanaka, H.; Hiraide, S.; Sugimoto, K.; Kubota, Y. Fast continuous measurement of synchrotron powder diffraction synchronized with controlling gas and vapour pressures at beamline BL02B2 of SPring-8. *J. Synchrotron Rad.* **2020**, *27*, 616–624. [CrossRef]
70. Izumi, F.; Ikeda, T. A Rietveld-analysis programm RIETAN-98 and its applications to zeolites. *Mater. Sci. Forum* **2000**, *321–324*, 198–205. [CrossRef]